21st Australasian Fluid Mechanics Conference
Adelaide, Australia
10-13 December 2018

Surface Pressure of Inclined Slender-Body Flows

S.-K. Lee and M. B. Jones

Defence Science and Technology Group, Melbourne, VIC 3207 AUSTRALIA

Abstract

This paper reports high-resolution surface-pressure maps obtained from inclined slender-body flows. The pressure maps are interpreted with the aid of an empirical model developed from an extensive flow-visualisation database. This model predicts flow separation on the leeward side of arbitrary axisymmetric slender bodies. The present findings show that, on the leeward side, the flow separation is in the vicinity of the local maxima in the time-averaged distribution of surface pressure.

Introduction

The surface flow over an inclined slender body produces very distinct separation lines [2–4]. These characteristic lines are of interest because they relate to the off-body wakes and the pressure forces acting on the body. An understanding of the separation lines and how they compare with the surface pressure can be useful, for example, to improve the dynamic control of slender-body type vehicles and to assist numerical modelling.

For the flow under consideration (figure 1), the separation lines are treated as transient, and the time scale is given by [2]:

$$t = \frac{x}{U_\infty \cos(\psi)}, \quad t^* = t\,\frac{U_\infty \sin(\psi)}{r(x)} = \frac{x}{r(x)}\tan(\psi), \qquad (1)$$

where $r(x)$ is the local body radius, ψ is the incidence angle and U_∞ is the free-stream velocity. The advantage of the scaling (1) is that it can be applied to any arbitrary slender bodies.

A recent flow-visualisation experiment and review study [3] show that, for a large collection of slender-body shapes at incidence ψ up to 35°, the scaling (1) provides a collapse of the leeward separation lines. These separation lines are the primary and secondary negative bifurcations (B_1^- and B_2^-) as shown, for example, in figure 1; they fall on the power laws [3]:

$$\Theta_{B_1^-} = 151.2(t^*)^{-0.190}, \ \Theta_{B_2^-} = 137.5(t^*)^{0.045}, \ t^* \geq 1.5. \qquad (2)$$

The azimuthal (Θ) locations of separations are independent of Reynolds number $Re_L = LU_\infty/\nu$ over the range $2.1\times10^6 \leq Re_L \leq 23\times10^6$ for a slender body of length L and a working fluid of kinematic viscosity ν. In figure 1, the narrow region of surface flow between B_1^- and B_2^- is known as the "separation envelope". The aim is to establish the time-averaged surface pressure for comparison with the separation envelope.

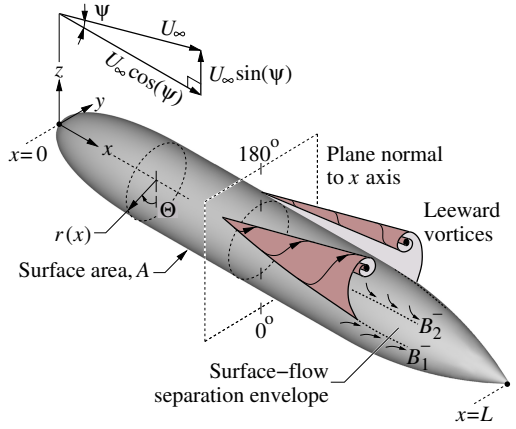

Figure 1. Flow separation on an inclined slender body in translation.

Slender-Body Geometry and Experimental Technique

The geometry used here consists of a NACA0018 nose of length $l_n/L = 0.23$, a cylindrical midsection of length $l_m/L = 0.47$ and a tapered tail of length $l_t/L = 0.30$. It has a fineness ratio $R = L/(2r_m) = 7.3$, a body length $L = l_n + l_m + l_t$ and the profile:

$$\frac{r(x)}{L} = \begin{cases} a_0\sqrt{\dfrac{x}{L}} - a_1\dfrac{x}{L} - a_2\left(\dfrac{x}{L}\right)^2 + \\ \qquad a_3\left(\dfrac{x}{L}\right)^3 - a_4\left(\dfrac{x}{L}\right)^4, & 0 \leq x \leq l_n, \\ \dfrac{1}{2R}, & l_n < x \leq L - l_t, \\ \dfrac{1}{2R} - \dfrac{1}{2R}\left(\dfrac{l_t}{L}\right)^{-2}\left(\dfrac{x}{L} - 1 + \dfrac{l_t}{L}\right)^2, & L - l_t < x \leq L, \end{cases} \qquad (3)$$

where $a_0 = 0.2322$, $a_1 = 0.1126$, $a_2 = 0.4097$, $a_3 = 0.4321$ and $a_4 = 0.2012$ define the shape of the nose; see figure 2.

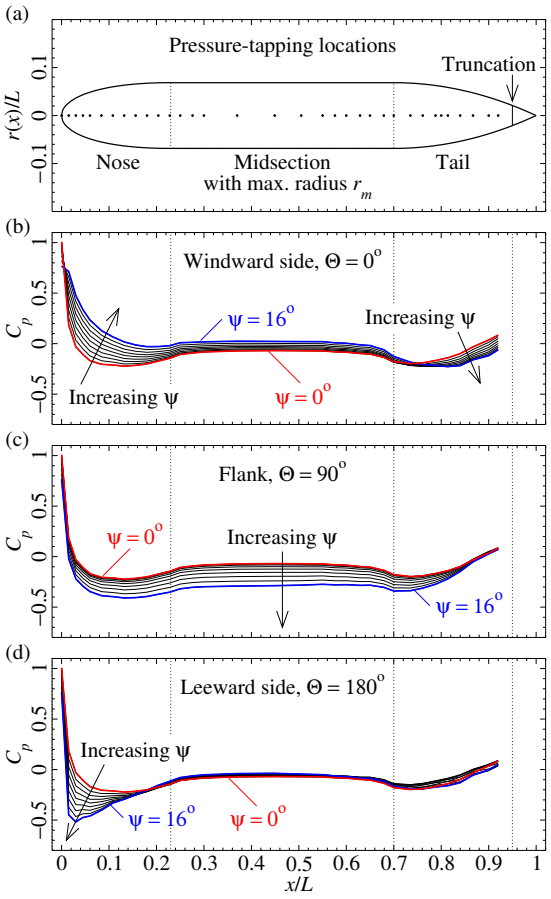

Figure 2. (a) Body geometry and locations of surface-pressure tappings. (b)-(d) Longitudinal distributions of surface pressure C_p, Eq. (4), at selected Θ locations for $\psi = 0°$ to 16° at incremental steps of 2°.

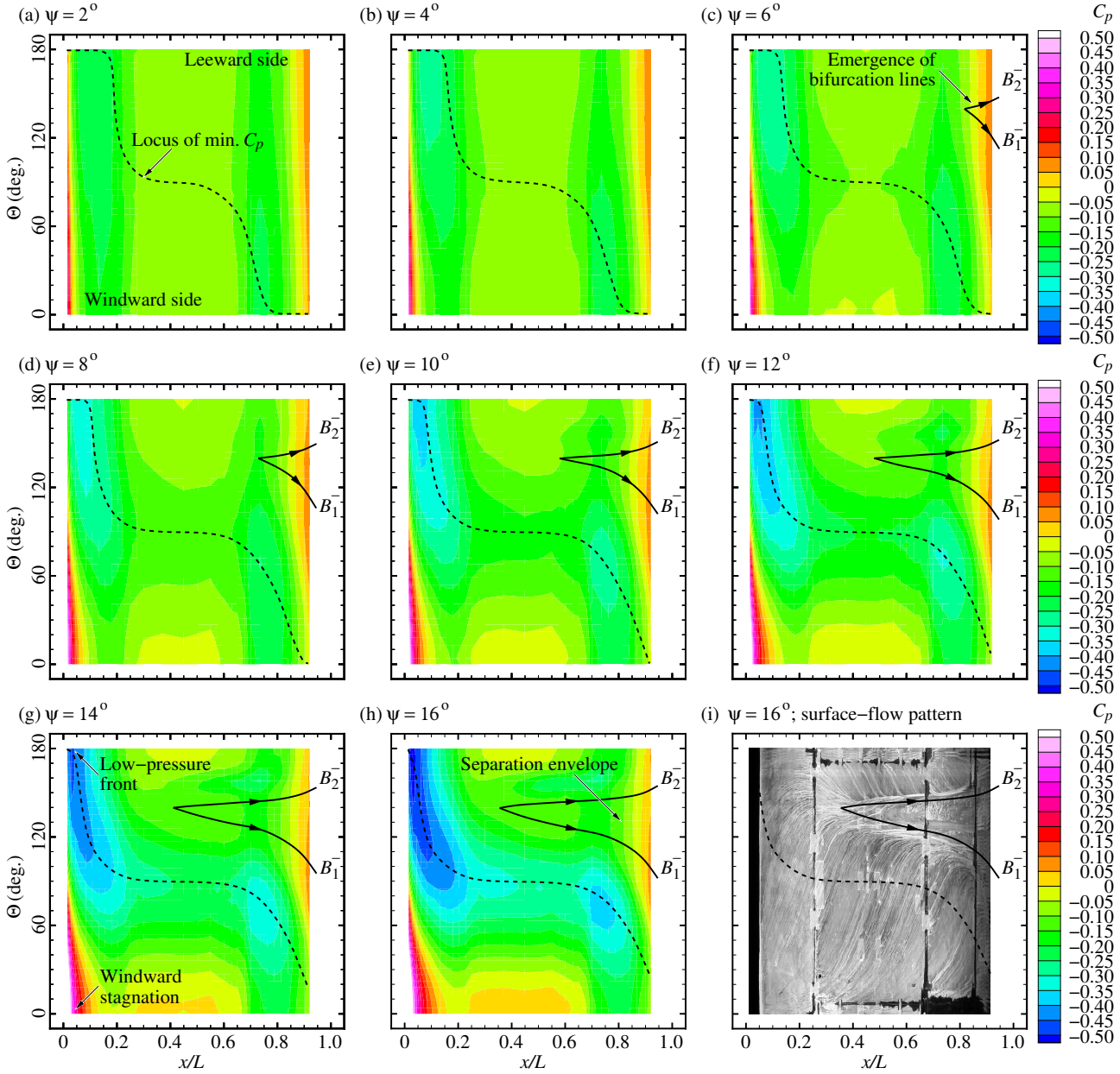

Figure 3. (a)-(h) Surface pressure C_p; the bifurcations B_1^- and B_2^- are modelled by Eqs. (1)-(3). (i) Example of a China-clay image for $\psi = 16^\circ$.

For testing in the low-speed wind tunnel at the Defence Science and Technology Group, a carbon-fibre composite body is manufactured with a length (L) of 2 m. The tapered tail is truncated at $x/L = 0.95$ to allow mounting on an automated sting-column rig. To monitor pitch and roll, an inclinometer (Jewel LCF-3000) is fitted inside the body; the standard errors are 0.013 ° in pitch and 0.046 ° in roll.

On each quadrant of the body, there is a row of 33 surface-pressure (p_s) tappings and 1 additional tapping at the tip of the nose; see figure 2(a). Inside the body, the tappings are connected to a series of miniature differential pressure (electronic DTC) scanners with an operating range of 1 kPa up to 35 kPa. The surface-pressure signals are captured by a commercial data acquisition system (MSS-8400) and are used to calculate the pressure coefficient:

$$C_p = \frac{p_s - p_\infty}{\frac{1}{2}\rho U_\infty^2}, \tag{4}$$

where ρ is the density and p_∞ is the static pressure of the free-stream. The wind-tunnel flow (U_∞) is operated at 60 m/s with $Re_L = 8 \times 10^6$. The pressure (p_s) at each tapping is sampled at 100 Hz and averaged over a period of 6 seconds. Pitch angles (ψ) are tested up to 16 °. To trip the flow, a circumferential ring of trip dots (diameter of 1.27 mm, thickness of 0.152 mm, and center-to-center spacing of 2.54 mm) is fixed at $x/L = 0.05$. The method of sizing the trip dots is from [1].

Surface-Pressure Distribution

Figures 2(b)-(d) provide the longitudinal distributions of pressure at different quadrants of the body. Inspection shows an increase in ψ produces a higher C_p on the windward side of the nose ($\Theta = 0^\circ$) and a lower C_p on the leeward side ($\Theta = 180^\circ$). The C_p along the flank ($\Theta = 90^\circ$) decreases with increasing ψ.

From a collection of longitudinal distributions of C_p such as in figures 2(b)-(d), it is possible to construct detailed maps of the surface pressure as shown in figures 3(a)-(h). This is achieved experimentally by rotating the axisymmetric body about its longitudinal (x) axis at incremental steps $\Delta\Theta = 4.5^\circ$, where each map contains a total of $33 \times 360^\circ/4.5^\circ = 2640$ pressure points.

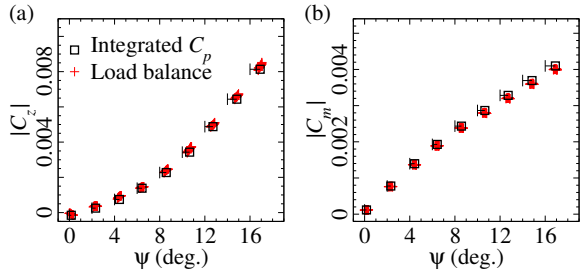

Figure 4. Comparison between integrated C_p and load-balance measurements; (a) side-force and (b) moment coefficients; the half error bars show the uncertainties in ψ (pitch) due to wind-on deflection.

For $\psi > 0\,^\circ$, the C_p maps are folded about the flow-symmetry plane (in the xz direction; see figure 1) to minimise scatter. For $\psi = 0\,^\circ$, the map is axisymmetric and is not shown here.

Comparison with Load Measurements

To check that the measurement grid is sufficiently fine, the pressure is integrated over the surface (area A) of the body to provide load estimates for comparison with strain-gauge data. Figure 4 shows, for example, a plot of the integrated C_p for pitch motion in the z direction (see figure 1); the side-force coefficient is

$$C_z = -\frac{1}{A}\int_0^L\int_0^{2\pi} C_p\, r\, \sin(\Theta)\; d\Theta\, dx \qquad (5)$$

and the moment coefficient about the nose (due to pitching) is

$$C_m = -\frac{1}{AL}\int_0^L\int_0^{2\pi} C_p\, r\, \left(x + \frac{dr}{dx} r\right) \sin(\Theta)\; d\Theta\, dx. \qquad (6)$$

For each nominal value of ψ, a total of 22 samples (+) are obtained from an internal (6-component Aerotech) strain-gauge balance; the scatter of the load-balance data in figure 4 is up to $\sim \pm 0.250 \times 10^{-3}$ for C_z and $\sim \pm 0.125 \times 10^{-3}$ for C_m.

In figure 4, the measured body pitch angle (ψ) takes into account the effect of wind-on deflection. For the largest angle $\psi = 16\,^\circ$, the deflection (monitored by the inclinometer) is no more than $1\,^\circ$, and the maximum difference between measurements obtained from integrating C_p and from the load balance is no more than 5% for C_z and 3% for C_m.

Comparison with Flow Visualisation

To assist interpretation, figure 3 includes the separation lines B_1^- and B_2^- modelled by Eqs. (1)-(3). For validation, figure 3(i) provides an example of a China-clay pattern to demonstrate flow separation over the body at $\psi = 16\,^\circ$. The process required the clay mixture to be exposed to the flow for a few minutes to dry before still photography. The $180\,^\circ$ view in figure 3(i) is constructed from longitudinal strips of the recorded images; this is achieved by rotating the body (at incremental steps of $5\,^\circ$) about its x axis with a fixed position of the still camera. For further details on the China-clay technique, see [3].

Figure 3 shows the lines B_1^- and B_2^- for $\psi \gtrsim 6\,^\circ$; they extend upstream of the tapered tail with increasing ψ and they define the separation envelope of the surface flow. The separation envelope is located leeward of the locus of minimum C_p. On the nose, the maximum C_p of the windward stagnation is diametrically opposite to the low-pressure front (see figure 3). By taking circumferential slices at selected x/L locations, figure 5 shows that the separation envelope (•–•) modelled by Eqs. (1)-(3) is in the vicinity of the local maxima or "plateaux" of C_p.

To further visualise the surface-pressure distribution, the C_p in figures 3(a)-(h) is replotted as a function of Eq. (1) in figures

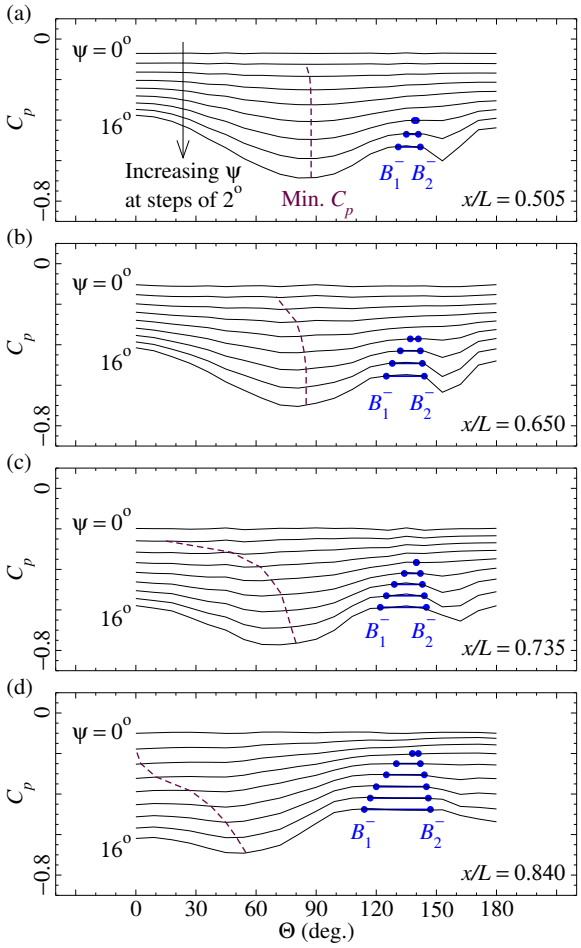

Figure 5. Circumferential distribution of C_p at selected x/L locations. The C_p contours for $\psi = 0\,^\circ$ are with no offset. For clarity, the successive contours for $\psi \geq 2\,^\circ$ are vertically offset at incremental steps $\Delta C_p = -0.05$. The loci of minimum C_p are shown as dashed lines. The separation envelope (•–•) is modelled by Eqs. (1)-(3).

6(a)-(h). Here, the time scale t^* increases with ψ, and as the flow separates the local maxima of C_p become more prominent. Figure 6(i) provides a further example which shows the effect of increasing ψ on selected contours "$C_p = -0.10$". A plot of the size of the separation envelope $\Theta_{B_2^-} - \Theta_{B_1^-}$ from the contours "$C_p = -0.10$" as a function of t^* in figure 7 shows close agreement with the power-law model (2), where the root-mean-square difference is $\simeq 9\%$.

Concluding Remarks

Time-averaged surface-pressure maps have been obtained from experiments on inclined slender-body flows to allow comparison with separation lines established from flow visualisation. Each map is constructed from a grid of $33 \times 360\,^\circ/4.5\,^\circ = 2640$ pressure points. For body incidence angles up to $16\,^\circ$, this experiment showed that the maximum difference between loads obtained from integrating surface pressure and from internal strain-gauge measurements is no more than 5%.

The most striking features of the surface flow are the negative bifurcations (B_1^- and B_2^-). They propagate upstream with increasing body incidence angle, and they define the separation envelope of the surface flow. Comparison with surface pressure showed that the separation envelope is in the vicinity of the local pressure maxima (or plateaux) of the leeward flow.

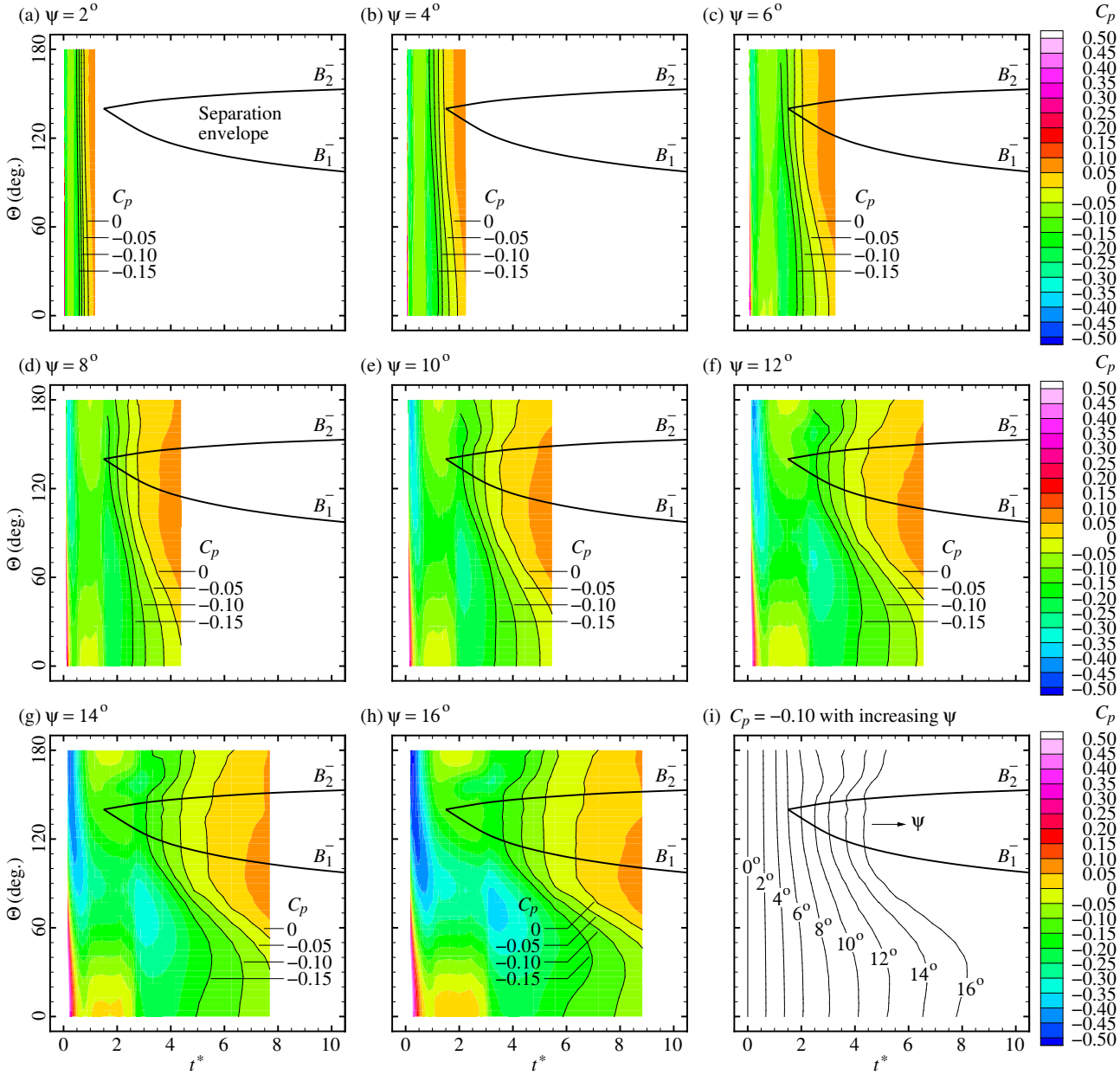

Figure 6. (a)-(h) Surface pressure (C_p) as a function of time t^*; the bifurcations B_1^- and B_2^- are modelled by Eq. (2). (i) Example of selected contours "$C_p = -0.10$" showing the effect of increasing incidence angle ψ.

Acknowledgements

Thanks go to Mr. Paul Jacquemin and to QinetiQ for wind-tunnel operation and technical assistance, including the plumbing of pressure ports on the test geometry. This work acknowledges the financial support from DST Maritime Division.

References

[1] Henbest, S. M. and Jones, M. B., *Transition on a generic submarine model*. Defence Science and Technology, 2018, in preparation.

[2] Jeans, T. L. and Holloway, A. G. L., Flow-separation lines on axisymmetric bodies with tapered tails, *J. Aircraft*, **47**(6), 2010, 2177–2183.

[3] Lee, S.-K., Longitudinal development of flow-separation lines on slender bodies in translation, *J. Fluid Mech.*, **837**, 2018, 627–639.

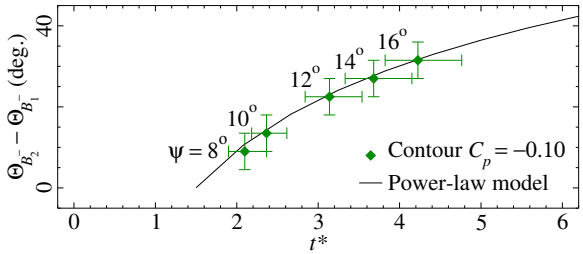

Figure 7. Comparison between the surface-flow separation envelope, $\Theta_{B_2^-} - \Theta_{B_1^-}$, determined from the plateaux of selected contours "$C_p = -0.10$" in figure 6(i) and from the power-law model (2). The error bars are defined by the resolution of the measurement grid for C_p.

[4] Wetzel, T. G., Simpson R. L. and Chesnakas C. J., Measurement of three-dimensional crossflow separation, *AIAA J.*, **36**(4), 1998, 557–564.